Journal of Power Sources 183 (2008) 182–192

Contents lists available at ScienceDirect

Journal of Power Sources

journal homepage: www.elsevier.com/locate/jpowsour

A numerical investigation of the effects of compression force on PEM fuel cell performance

Z.Y. Su[a,*], C.T. Liu[b], H.P. Chang[c], C.H. Li[b], K.J. Huang[c], P.C. Sui[d]

[a] Department of Information Management, Chia Nan University of Pharmacy & Science, Tainan, Taiwan
[b] Fuel Cell R&D Department, Delta Electronics Incorporation, Taoyuan, Taiwan
[c] Chung Shan Institute of Science and Technology (CSIST), Armaments Bureau, M.N.D., Taiwan
[d] Institute for Integrated Energy Systems, University of Victoria, Victoria, BC,V8W 3P6 Canada

ARTICLE INFO

Article history:
Received 9 March 2008
Received in revised form 22 April 2008
Accepted 22 April 2008
Available online 3 May 2008

Keywords:
PEMFC
Fuel cell
GDL
Porosity
Compression force
Rib

ABSTRACT

In the present study we report on numerical investigations into the effects of compression on the performance of a unit cell. The focus of this study is how the transport properties of the gas diffusion layer (GDL) material, specifically porosity and permeability, affect numerical predictions of cell performance. Experimental data of porosity and permeability of uncompressed and compressed GDLs were obtained using a porometer, and used in numerical simulations. A 3D model with two parallel channels and an membrane electrode assembly (MEA) is constructed for the calculations. Three different configurations of transport properties were tested, i.e. uniform uncompressed GDL properties, uniform compressed GDL properties, and non-homogeneous GDL properties. It is found that the non-homogeneous case shows noticeable differences in predicted cell performance. For the non-homogenous case, simulations with a pressure difference between two cathode channels were carried out to gain insight into the effect of cross-channel flow on the overall prediction of cell performance. We found that the cross-channel flow changes local current density distribution primarily on the high-pressure channel. The present study demonstrates the importance of the proper use of transport properties for the compressed portion of the GDL.

1. Introduction

The gas diffusion layer (GDL), typically made of carbon paper or carbon cloth and coated with Teflon and binder materials, is a key component in a proton exchange membrane fuel cell (PEMFC) because of its central role in transport processes in the unit cell. The GDL has multiple functions: it serves as a support for the catalyst layer and the membrane, and as a conductor for electricity and heat, and provides pathways for species transport.

Fig. 1 shows a cross-section of the unit cell with the membrane electrode assembly (MEA) sandwiched between two flow field plates. The GDL is in contact with the bipolar plate on the one side and with the catalyst layer on the other. In typical plate-and-frame designs of PEMFC, the bipolar plate has flow channels for gas distribution and land area, termed 'ribs', that remain in contact with the GDL for electric conduction. In order to achieve optimum performance, a uniform distribution of gas species on the catalyst layer, and minimum electrical and thermal resistance are required. When unit cells are assembled into a stack, a compression force is applied to the entire stack to minimize gas leakage through the unit cell. However, these requirements often conflict, which calls for careful design of the bipolar plate.

The characteristics of the GDL as a porous medium have significant impact on cell performance. Important factors include volumetric properties such as porosity, permeability, tortuosity, thermal and electrical conductivity, and surface properties such as wettability and roughness. The effects of these properties on cell performance have been published in literature [1–12]. In general, mass transport of gaseous species driven by diffusion is affected by porosity and tortuosity, whereas mass transport due to pressure difference is affected by permeability, e.g. cross-channel gas flow and liquid water flow from catalyst layer to gas channel [13,14]. Thermal and electrical conduction are comparable because of the fact that both transport processes take place in similar (solid) phase, although for thermal conduction the binder and gas in the pores also make a contribution, in addition to that made via the carbon fibers. The thermal and electrical contact resistances of the GDL with the bipolar plate are sensitive to the surface roughness of the GDL. Transport of liquid water in the GDL has been the focus of

* Corresponding author. Tel.: +886 6 2664911x5305; fax: +886 6 3660607.
E-mail addresses: zysu@mail.chna.edu.tw (Z.Y. Su), ANDREW.JD.LIU@delta.com.tw (C.T. Liu), hsinping650204@yahoo.com.tw (H.P. Chang), CHARLES.LEE@delta.com.tw (C.H. Li), kjhuang1@ms3.hinet.net (K.J. Huang), jsui@uvic.ca (P.C. Sui).

0378-7753/$ – see front matter © 2008 Elsevier B.V. All rights reserved.
doi:10.1016/j.jpowsour.2008.04.060

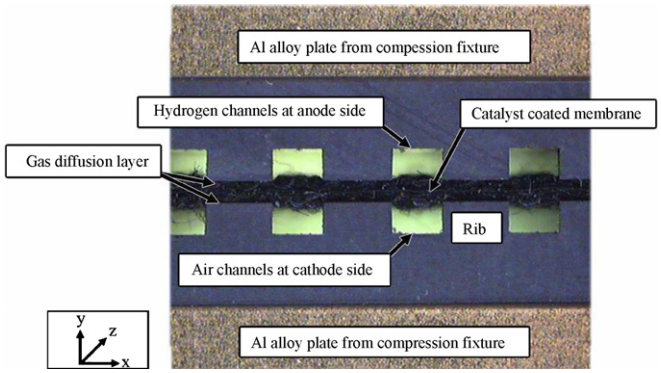

Fig. 1. Cross-section area of single fuel cell.

numerous papers, e.g. Refs. [15–17]. The transport of liquid water is mostly dependent on the wettability of the GDL materials and the connectivity of the pore network. Since both liquid water and gaseous species occupy the same pore volume, transport of liquid water has a profound impact on the mass transfer of gas within the GDL. The mass, heat and electron transport processes in the GDL are coupled mainly due to the rib/channel configuration that causes a skewed distribution of mass, heat and electron flows [18,19]. The problem is further complicated when deformation occurs in the GDL due to compression force exerted on the stack. The material properties of both the rib area and the channel area of the GDL may change dramatically due to such deformation.

Models and simulation tools have been developed to facilitate analysis of the complex problems involved in understanding the GDL, e.g. Ref. [20]. Uniform material properties for the GDL are adopted by most authors [21–26]. In these numerical simulations, constant and uniform transport properties were set for the GDL material under the ribs and the channels. Such cases are referred to as *homogeneous* cases in the present study. Apparently, the *homogeneous* case cannot predict the effects of compression force on cell performance. There have been few systematic investigations of the effects of non-uniform transport properties of the GDL due to compression. Gurau et al. [27] developed a one-dimensional half-cell model that considered non-uniform GDL properties to account for the fact that the pores might be partially filled with liquid water. Chu et al. [28] developed a one-dimensional half-cell model and studied the impact of non-uniformity GDL porosity with four different continuous functions of the position (constant, linear, convex, and concave exponential function). Roshandel et al. [29] reported a two-dimensional model that simulates the porosity change of the GDL after compression. They used a composition function in the form of $\mathrm{Sin}^{2n}(x)$ to describe the effect on cell performance of a change in the porosity of the GDL. Zhou et al. [30] investigated the effect of clamping force on the performance of PEMFC with an interdigitated gas distributor, considering the interfacial contact resistance, the non-uniform porosity distribution of the GDL, and the GDL deformation. In a recent work, Zhou and Wu [31] included transport of liquid water in the model and reported simulation results in a 2D configuration. The effects of non-uniform compression of the GDL under the channel/rib structure of flow-filled plate on the temperature distribution in the PEMFC is studied in Hottinen and Himanen [32]. Recent work of Nitta et al. [33] and Hottinen et al. [34] reported more thorough experimental and numerical investigations of this issue.

In the present study we report on the results of numerical investigations when the change of the transport properties of GDL due to compression force is considered. Different porosity and permeability measured from compressed and uncompressed GDL material are assigned to the rib and channel areas of the GDL, respectively. This case is termed the *non-homogeneous* case in the following discussion. The objective of the present study is to investigate the effects of compression force on cell performance. A three-dimensional computational model using properties and parameters validated with experimental data is constructed to assess the sensitivity of predicted results when realistic, non-uniform GDL properties are used.

2. Characterization of the GDL

Fig. 1 shows a cross-section area of a unit cell sandwiched by two pieces of plates as the compression fixture. The GDL under

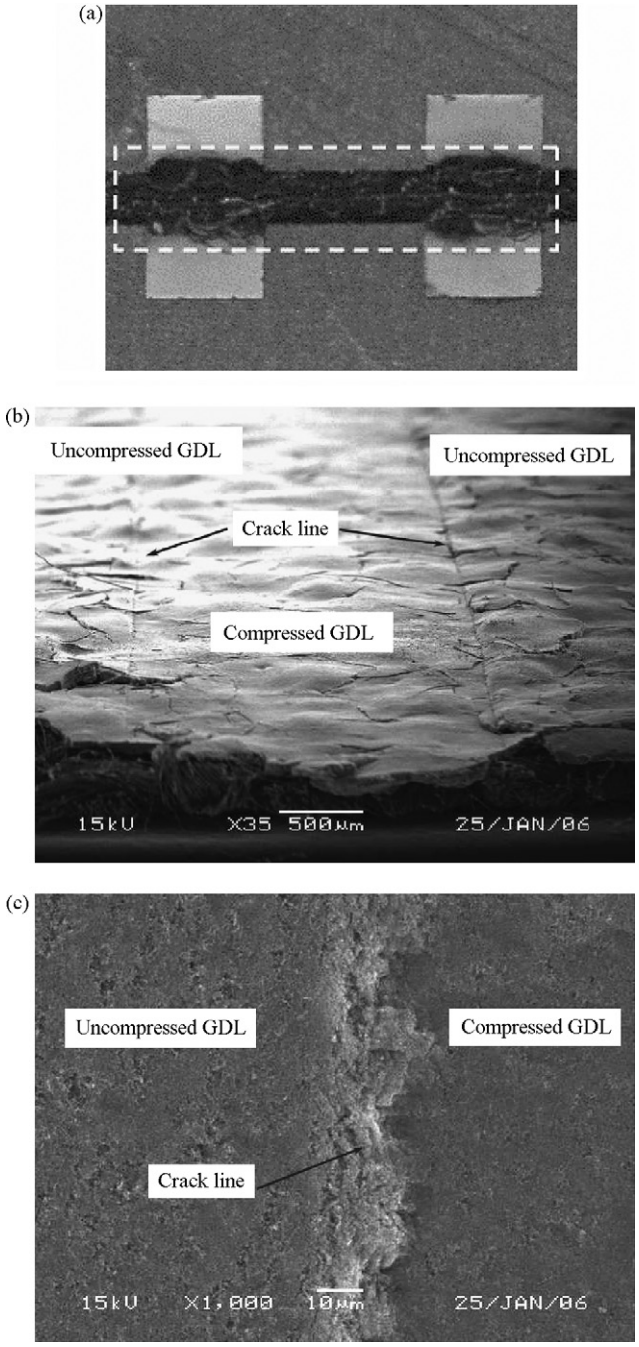

Fig. 2. SEM photo of the compressed and uncompressed GDL as (a) obersvered zone; (b) 500 μm; (c) 10 μm.

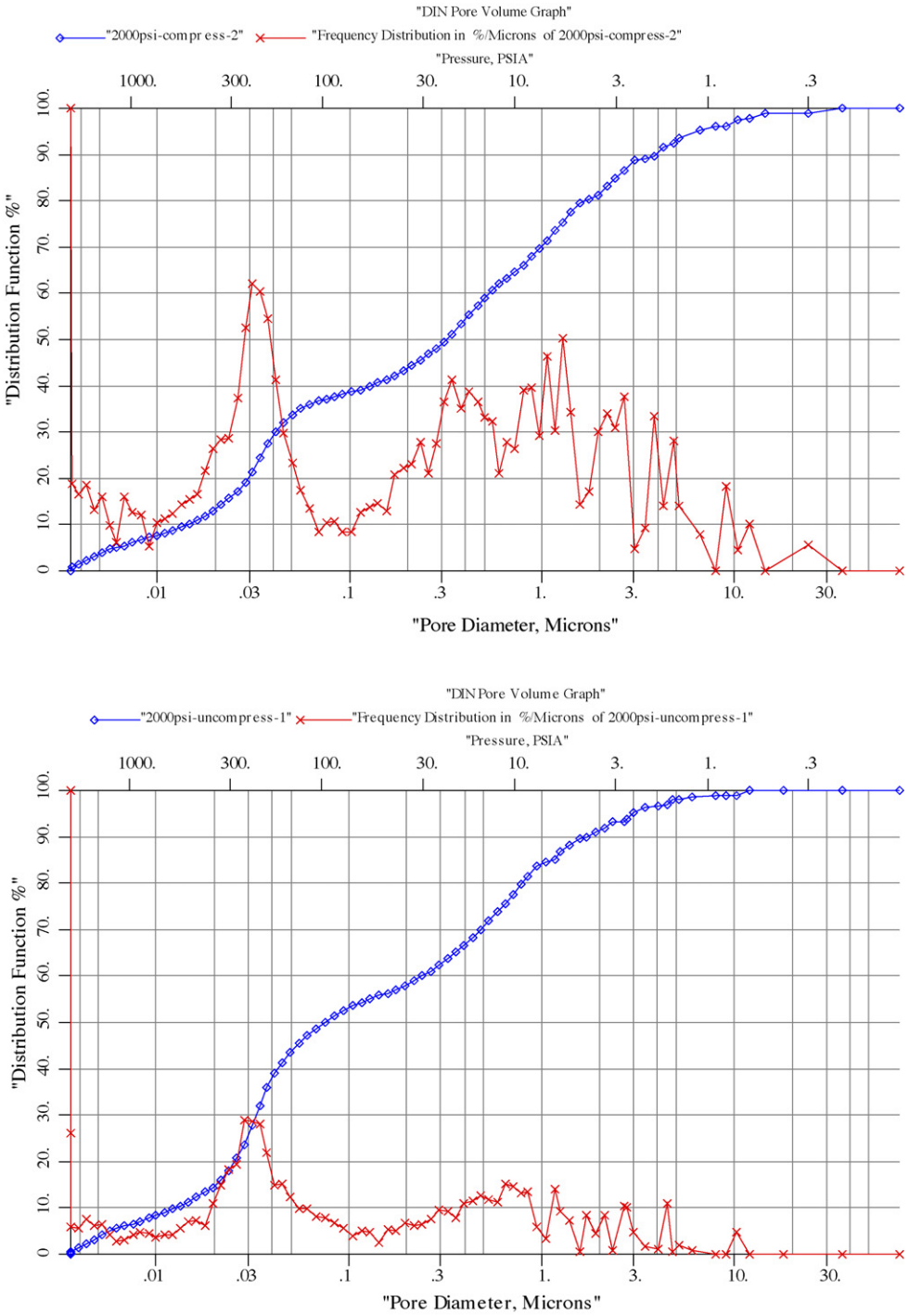

Fig. 3. Pore size distribution (left: uncompressed GDL; right: compressed GDL).

the rib area appears to be thinner than the portion in the channel area. Since the GDL serves multiple purposes of transport (reactant gases, product water, electrons, and heat), characterization of the GDL material in both regions will help modeling and simulations of the transport in the GDL. In the present study we measure the permeability and porosity of the compressed (under the rib) and uncompressed (under the channel) zone of the GDL and use the measured properties in numerical simulations for prediction of cell performance due to compression.

The bipolar plate and gasket on either side of the MEA are bolted together under significant clamping force. This enables optimum gastight during fuel cell assembly. GDL deformation depends on the thickness, form, and material of the gasket and clamping force during fuel cell assembly. However, compression force is known to change the porous medium of the electrode and GDL. The magnitude of the compression force affects directly diffusion and permeability of the reactant gases in the compressed GDL. A high compression force increases mass transfer resistance in the compressed GDL, which has lower porosity than uncompressed GDL. Conversely, a low compression force increases the contact resistance between the GDL and the bipolar plate, as well as gas leakage.

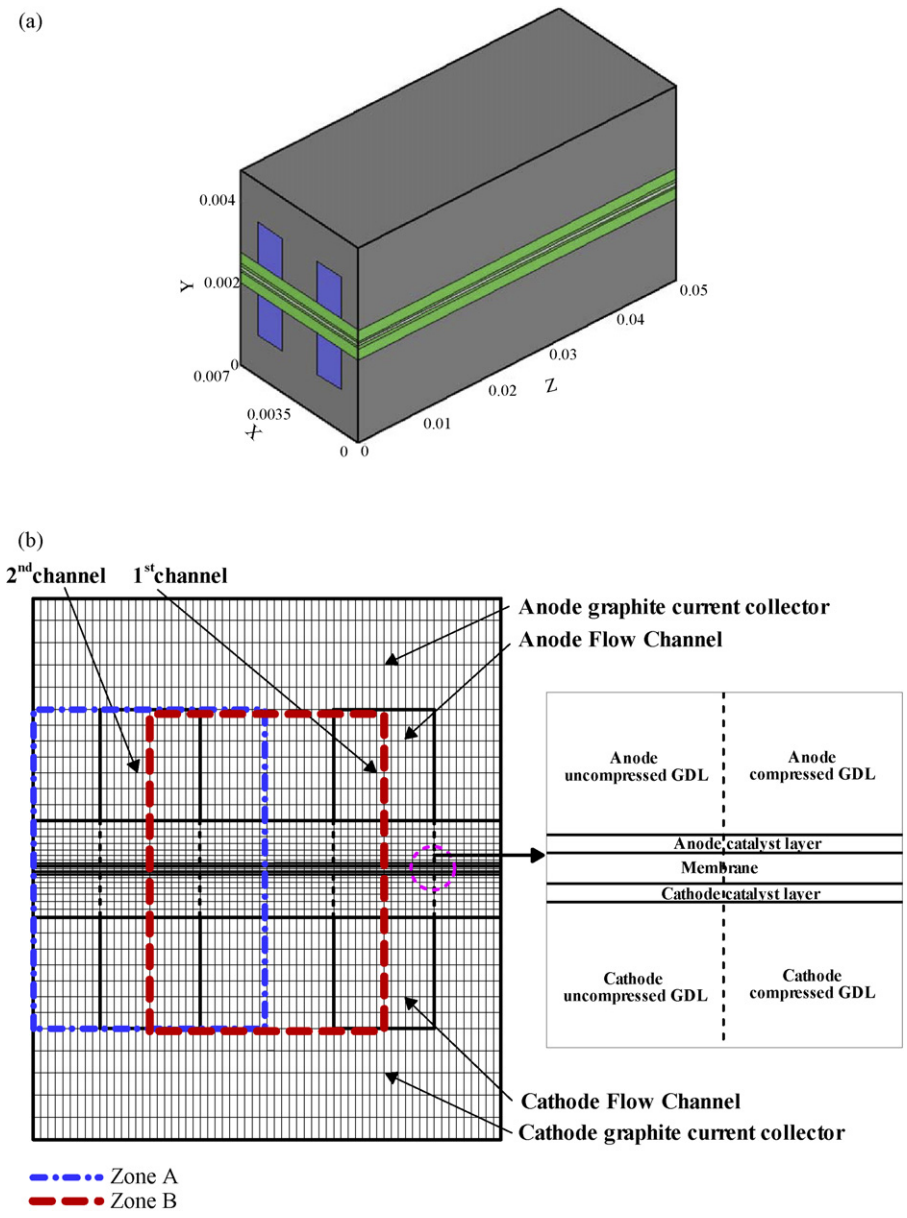

Fig. 4. Computational domain (a) and mesh (b) in the *XY* plane.

A scanning electron microscope (SEM, JSM-5610LV; JEOL) was employed to observe the changes in the GDL surface microstructure compressed by the rib area of the bipolar plate. The procedure of applying compression force to a fuel cell assembly is illustrated in Ref. [35]. Fig. 2(a) shows a cross-section of a single cell, showing two gas channels and one rib in the image. A close-up of the GDL surface after compression by the rib is shown in Fig. 2(b) and (c), which depict a top view of the GDL surface for the region marked with a dotted box in Fig. 2(a). It is clear that, in the zone under compression by the rib, there are two cracks on the GDL surface. After the fuel cell is assembled, the physical characteristics of the compressed area of the GDL become different than those of the uncompressed area. The GDL surface of the area that is exposed to the rib clearly contains more cracks. In Fig. 2(a), the GDL exposed to the gas channel is not under compression and only a small portion protrudes into the channel. Under the rib of the bipolar plate, the GDL is thinner than the channel portion. Fig. 2(b) shows the GDL with microporous coating on one side. Two crack lines may be seen on the microporous surface. Fig. 2(c) shows a close-up of the area near a crack line with a depth of approximately 10–20 μm. In the present study, carbon black with 30 wt.% PTFE (Teflon 30J, Dupont™) was coated on the carbon cloth (CPW-003 Textron) to make the GDL. The properties of uncompressed GDL were measured and used to represent the uncompressed zone in an assembled fuel cell, i.e. the portion of GDL facing the gas channel. For the properties representing the material under the rib, data was collected using the portion of GDL material compressed by the solid rib area during fuel cell assembly.

The permeability data of the compressed and uncompressed GDL were measured by a capillary flow porometer (Porous Material, Inc. CFP-1100-AEX). The porosity of the *compressed* and the *uncompressed GDL* was measured by a water intrusion porosimeter (Porous Material, Inc.), which measured the intrusion volume of water into the hydrophobic pores of the material as a function of pressure applied on water. Information of pore size distribution was deduced from the pressure data. In the present study, an average

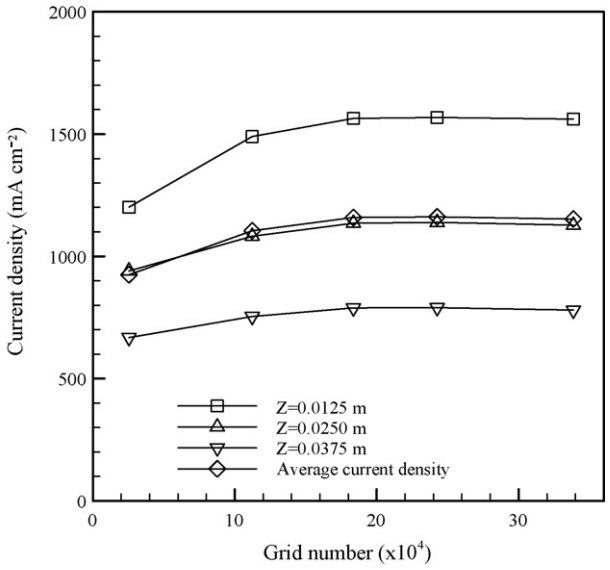

Fig. 5. Predicted current density profiles vs. number of grid.

of three to five specimens were measured and data were calculated to obtain a mean average porosity and permeability value. Measured data with these samples were within 5% error. The principles for these measurement techniques and data reduction can be found in Refs. [36,37]. The sampling principle involved comparing the characteristics of the dry and wet samples. A wetting liquid is first allowed to spontaneously fill the pores in the sample and a non-reacting gas is then introduced to displace the liquid from the pores. The gas pressure and flow rates through the dry and wet samples are accurately recorded. The gas pressure required for removing liquid from the pores and causing gas to flow is given by

$$D = \frac{4\gamma \cos\theta}{P} \quad (1)$$

where D is the pore diameter, γ is the surface tension of liquid, θ is the contact angle of liquid, and P is the pressure difference between liquid and gas. A pore size distribution function, f is defined as

$$f = -\frac{\mathrm{d}[100 \times (\mathrm{Fw}/\mathrm{Fd})]}{\mathrm{d}D} \quad (2)$$

Table 1
Flow channel dimensions and inlet conditions used in simulations

Parameter	Value
Channel length (mm)	50
Channel width (mm)	1.5
Channel depth (mm)	1
Solid rib area width (mm)	2
Gas diffusion layer thickness (mm)	0.3
Membrane thickness (mm)	0.05
Catalyst layer thickness (mm)	0.03
Membrane porosity	0.28
Membrane ionic conductivity ($\mathrm{S\,m^{-1}}$)	17
Electrode electronic conductivity ($\mathrm{S\,m^{-1}}$)	570
Membrane thermal conductivity ($\mathrm{W\,(m\,K)^{-1}}$)	0.455
Anode mass flow rate ($\mathrm{kg\,s^{-1}}$)	1.79×10^{-7}
Cathode mass flow rate ($\mathrm{kg\,s^{-1}}$)	1.28×10^{-6}
Hydrogen stoichiometric ratio	1.2
Air stoichiometric ratio	2
Anode hydrogen mass fraction	0.174
Anode water vapor mass fraction	0.826
Cathode oxygen mass fraction	0.195
Cathode nitrogen mass fraction	0.645
Cathode water vapor mass fraction	0.16

The pore size distribution function calculated from the variation of the flow rate with the differential pressure for through-plane flow, shown in Fig. 3. The area under the distribution curve in a given pore diameter range yields the percentage of flow through pores in that size range. In the present study, the porosity measured was 0.42 and 0.64 for the *compressed* and *uncompressed GDL*, respectively. The permeability was measured to 6.42×10^{-13} and 3.64×10^{-11} $\mathrm{m^2}$ for the *compressed* and *uncompressed GDL*, respectively. These values were used in the computer simulations to be discussed later.

3. Mathematical formulation and numerical simulations

3.1. Assumptions

The reaction of the fuel cell is complex, including electrochemical reactions, hydrodynamics, phase changes, heat transfer, and mass transfer. In order to carry out the numerical simulation and analysis, effective simplifications and assumptions must be made. The following are the key assumptions of this model:

(1) The gas mixture is a perfect gas.
(2) Steady state.
(3) Constant cell temperature.
(4) Laminar flow and incompressibility, because the gradient is of very small pressure.
(5) The porous medium is isotropic and homogeneous.
(6) Single phase flow that neglects the existence of the liquid water.
(7) Deformation of the porous medium is ignored (shrinks and expands).
(8) The reactant is not permeable through the proton exchanges the membrane.
(9) The Butler–Volmer equation controls electro-chemical dynamics.

A commercial software, CFD-ACE+, is used in the present study. Mathematical formulation of the fuel cell module of this software can be found in Mazumder and Cole [38].

3.2. Computational domain and mesh

A computational domain of a double-channel configuration is adopted to simulate transport in a single cell and to investigate the effect of compression pressure on cell performance. Fig. 4 shows the geometry and computational domain of the double-channel. The dimensions of the flow channel are 50 mm (L) × 1.5 mm (W) × 1 mm (H). The dimensions of the GDL are 50 mm (L) × 3.5 mm (W) × 0.3 mm (H).

Verification of grid independence for the numerical solutions was performed to confirm the accuracy of the computational results. Fig. 5 shows the relationship between the grid number and current density along with the channel (Z-axis). Local current density along the channel and the average plane current den-

Table 2
The GDL characteristics used in the simulations

Properties	Case type		
	Homogeneous(c)	Homogeneous(u)	Non-homogeneous
Rib area			
Porosity	0.42	0.64	0.42
Permeability ($\mathrm{m^2}$)	6.42×10^{-13}	3.64×10^{-11}	6.42×10^{-13}
Channel area			
Porosity	0.42	0.64	0.64
Permeability ($\mathrm{m^2}$)	6.42×10^{-13}	3.64×10^{-11}	3.64×10^{-11}

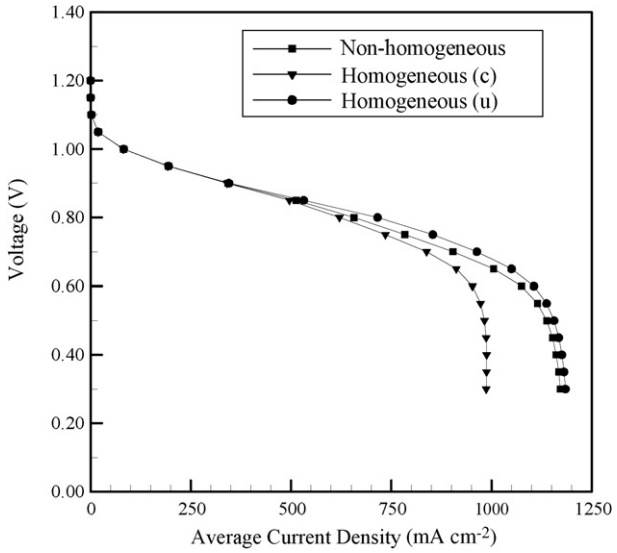

Fig. 6. Predicted polarization curve and power for homogeneous(c), homogeneous(u), and non-homogeneous cases.

sity were computed to evaluate the grid independence: when the grid number reaches 242,550 grids, the variation of the current density trends towards stability at $Z = 0.0125$ m. The variation of the current density is not influenced by further increases in the grid number. The results of the other positions are similar too. There is 0.42% of difference in predicted results between the cases when 242,550 and 338,550 cells were used in the domain, respectively. The computational domain with 242,550 cells was used throughout the simulations reported in this paper unless otherwise noted.

3.3. Boundary conditions and properties

Table 1 lists the gas composition and channel dimensions used in the computations. The anode gas mixture contains hydrogen and water vapor and the cathode gas mixture contains oxygen, nitrogen, and water vapor. Mass flow rate with known gas composition is prescribed for all channel inlets. Fixed pressures are set for the channel outlets. Table 2 lists the GDL properties used in the simulations. Two *homogeneous* cases are studied, the *homogeneous(c)* case, which uses properties of a *compressed GDL* material in the calculation, and the *homogeneous(u)* case, which uses properties of a *raw GDL* material. For the *non-homogenous* case, porosity and permeability data were used in their corresponding zone in the computational domain. For the *non-homogeneous* case, two outlet pressure conditions are tested to investigate the effect due to cross-channel flow. The baseline case has identical pressure for all outlets, i.e. $P_{A1} = P_{A2} = P_{C1} = P_{C2} = 100$ kPa. In the different pressure case, only the cathode outlet pressure is varied from $P_{C1} = 101$ to 103 kPa while all other outlets are kept the same pressure as the baseline case.

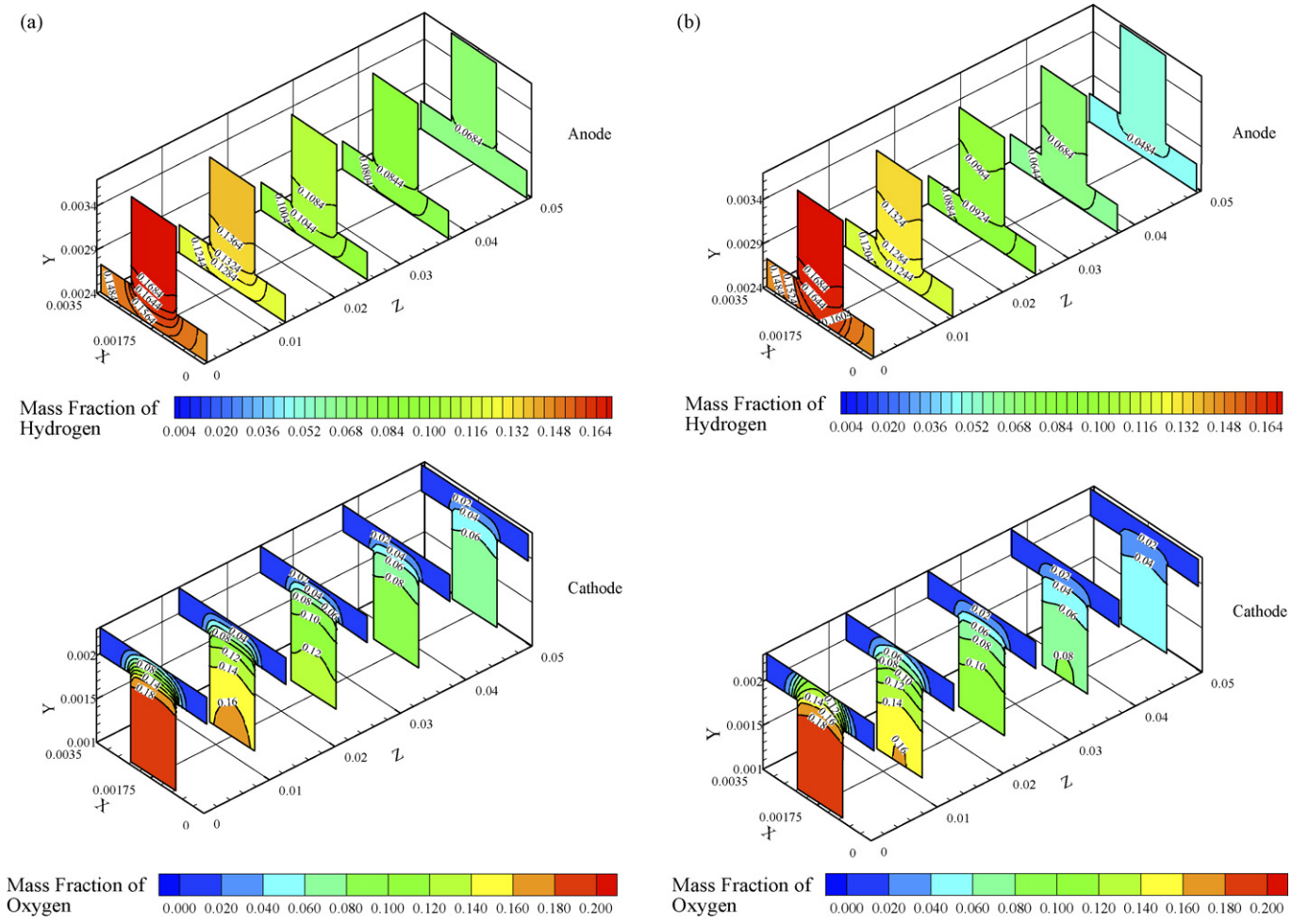

Fig. 7. Predicted mass fraction of reactant gases for two different GDL cases: (a) homogeneous(c); (b) non-homogeneous.

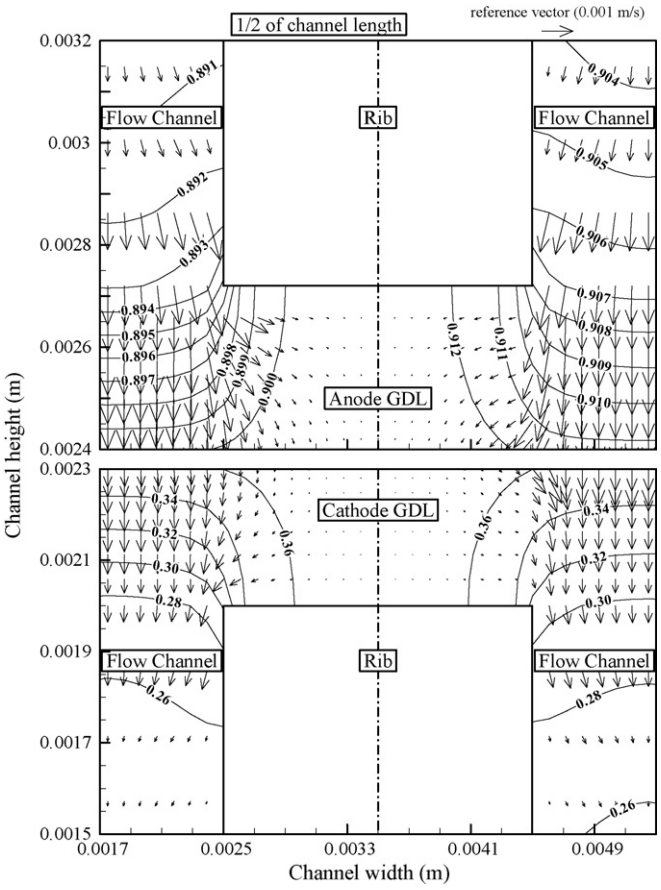

Fig. 8. Predicted velocity vector and mass fraction of water vapor (Z = 0.025 mm) left-half: homogenous(c); right-half: non-homogeneous.

4. Results and discussion

The variation of porosity and permeability in the GDL is expected to primarily affect the transport of reactant gases in the MEA. When the pressure of the two adjacent gas channels is the same, the transport of gas species is primarily dominated by mass diffusion, which is related to GDL porosity, because convective flow due to pressure difference between the channels is minimal. The effect due to variable permeability becomes important when there exists a pressure differential between adjacent gas channels. In Section 4.1, numerical investigations on the effect of GDL properties on predicted cell performance carried out for gas channels with the same inlet pressure are discussed. In Section 4.2, numerical results for the non-homogeneous case with different inlet pressure are compared.

4.1. Homogenous versus non-homogeneous GDL properties

Fig. 6 compares the predicted polarization curves for the *homogeneous(c)*, *homogeneous(u)*, and *non-homogeneous* cases. The inlet pressure of adjacent gas channels are set the same. For cell voltage above 0.9 V, one can see that all polarization curves are very close because the overpotential in this regime is dictated by the activation loss, therefore ohmic loss and potential loss due to mass transport are negligible. For cell voltage below 0.4 V, the polarization curves show effects due to mass transport limitation, which eventually results in an abrupt drop of cell potential at higher current density. The limiting current density extrapolated from these curves for the *homogeneous(c)*, *homogeneous(u)*, and *non-homogeneous* cases is 0.995, 1.20, and 1.175 A cm^{-2}, respectively. It is noted that for both the *homogeneous(u)* and *non-homogeneous* cases, the porosity immediately under the gas channel region is the same. Comparing the limiting current density value for these cases, one can see that apparently the porosity for the portion of the GDL underneath the gas channel has more impact on the mass transfer.

Fig. 7(a) and (b) compare the distribution of mass fraction of reactant gases for *homogeneous(c)* and *non-homogeneous* cases at 0.4 V. Computational results of zone A of Fig. 4(b) are shown in these figures. The GDL region underneath the channel area has a higher porosity for the *non-homogeneous* case, therefore the reactant gas sees less resistance. The results show an overall higher consumption rate of the reactant gases, hence a higher current density, along flow channel for the *non-homogeneous* case.

The velocity vectors on the X–Y plane and contours of water mass fraction at Z = 0.025 m for the *homogeneous(c)* and *non-homogeneous* cases are shown in Fig. 8. Computational results of zone B of Fig. 4(b) are shown in this figure. Because for both cases the computational results are symmetrical with respect to the rib centerline, the results are placed side by side to facilitate comparison. One can see for the cathode side, the net flow of the gas mixture is from the GDL to the gas channel, whereas for the anode side the net flow is from the gas channel to the GDL. It is noted that the velocity for each species is a result of the fluid velocity and diffusion velocity, which is expressed as a gradient of the mass fraction. For both cases one can see that in the channel region the velocity component in the XY plane is small because in the gas flow the axial direction (Z-coordinate) is dominating. For the flow under the rib in the GDL, the *non-homogeneous* case shows slightly lower velocity of the flow in the GDL between the portion under the channel and under the rib because of their dissimilar properties. More stratification of water concentration near this area is also observed for the *non-homogeneous* case.

Fig. 9 compares predicted current density profiles at channel centerline (x = 0.00175) along the flow channel for the *homogeneous(c)* and *non-homogeneous* cases. The current density shown in Fig. 9 is averaged over the rib-land length, thus it is different from that shown in Fig. 6, which is averaged over the MEA area of the entire domain. The average current density for the *homogeneous(c)* and *non-homogeneous* case, cf. Fig. 6, is 993.5 and 1161.3 mA cm^{-2}, respectively, a difference of 14.4%. A considerable difference for Z = 0.025–0.05 m is noted. For both cases, only the

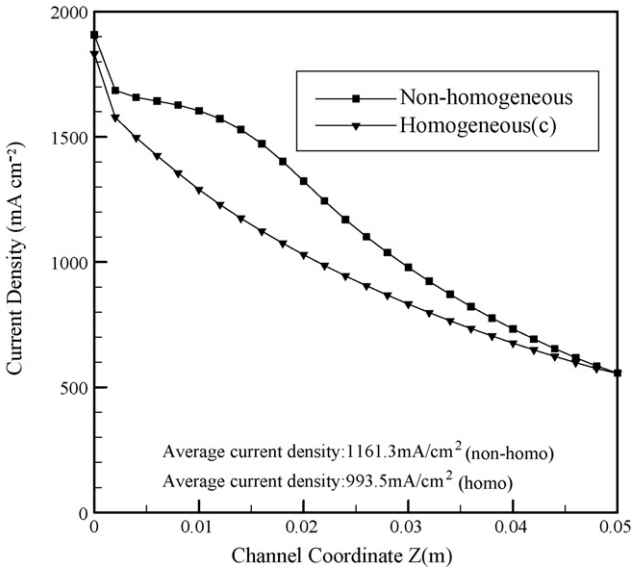

Fig. 9. Predicted current density profiles for different GDL properties.

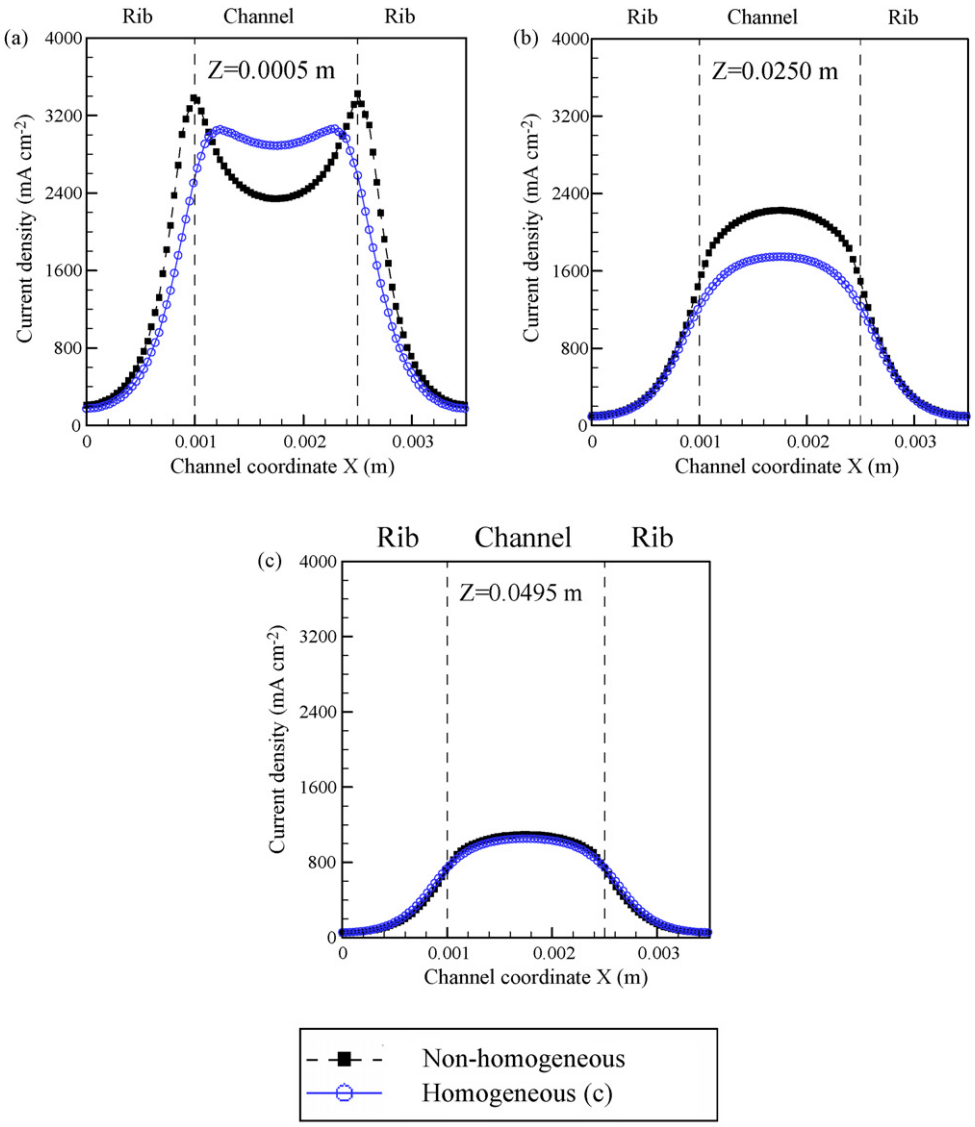

Fig. 10. Predicted current density in *Y*-direction for homogenous(c) and non-homogenous cases.

portion of the GDL underneath the rib has different porosities, i.e. the *non-homogeneous* case the porosity is 52% higher of that for the *homogeneous(c)* case. Therefore the reactant gases diffusing through the GDL are greater for the *non-homogeneous* case, resulting in a higher current density. At $Z = 0.0125$ m, the predicted current density of the *homogeneous(c)* and *non-homogeneous* cases are 1216 and 1562 mA cm^{-2}, respectively. At $Z = 0.025$ m, the current density of the *homogeneous(c)* and *non-homogeneous* case are 925 and 1136 mA cm^{-2}, respectively. Both predictions demonstrate that higher porosity of the GDL results in a better transport of the reactant gases and consequently a higher current density when mass transport becomes limited. At $Z = 0.045$ m, variation of the current density along the flow channel is similar in both cases.

The distribution of current density along cross-section area of the flow channel calculated using the *homogenous(c)* and *non-homogenous* cases is illustrated in Fig. 10 for three axial (Z) locations. Computational results of zone A of Fig. 4(b) are shown in this figure. For the *non-homogeneous* case, the distribution of current density is a concave curve, shown in Fig. 10(a). With this case the predicted current density near the border between the rib and the flow channel (3371 mA cm^{-2}) is higher than the current density of the central position (2341 mA cm^{-2}), cf. Fig. 10(a), a difference of about 30.6%. (The maximum current density occurs near the corner of the rib. This is a balance of mass transfer resistance in the GDL and the electrical resistance in the GDL material.) An implication of the highly non-uniform current density near the corner of the rib is that hot spots may occur and damage the MEA. The current density of other position drops significantly to about 211 mA cm^{-2} near the symmetry line of the rib. Further downstream the flow channel, cf. Fig. 10(b), the profile of current density resembles a bell-shape curve. The difference in the maximum current density predicted with the *homogeneous(c)* and the *non-homogeneous* case is about 27.4% for at $Z = 0.025$ m. Interestingly, the current profiles become similar near the channel outlet, cf. Fig. 10(c). In this case, the gas concentration predicted by both cases is similar.

Fig. 11 compares predictions of oxygen mass fraction at the cathode catalyst layer as function of current density for the *homogeneous(c)* and *non-homogeneous* case. There is a noticeable difference at high current density conditions. Under high loads, the current density distribution is influenced by variation of oxygen concentration along the flow channel. When the oxygen mass fraction is 0.1, the current density of the *non-homogeneous* case (438 mA cm^{-2}) is

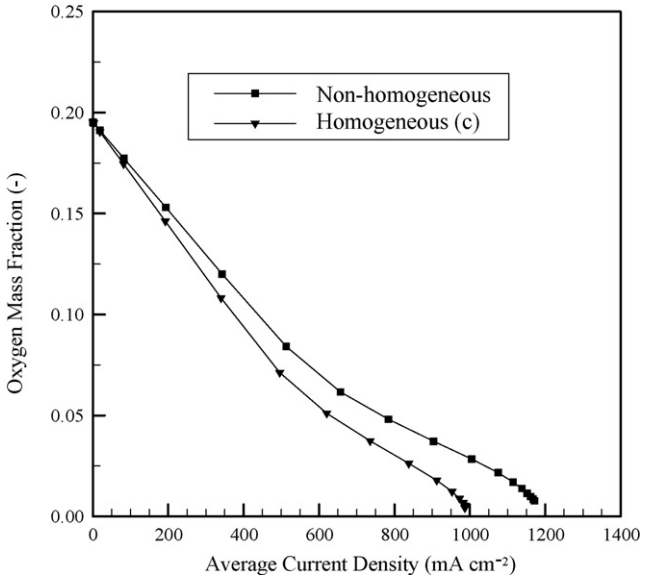

Fig. 11. Oxygen mass fraction at the cathode catalyst layer as function of current density for homogeneous(c) and non-homogeneous cases.

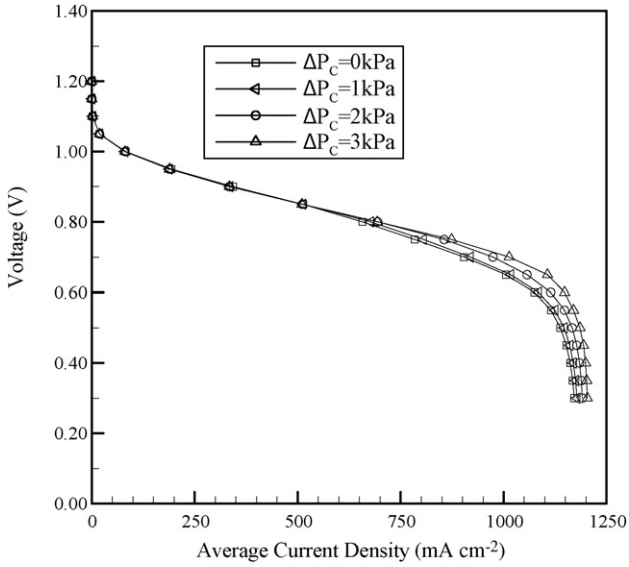

Fig. 12. Predicted polarization curve and power of the non-homogeneous case for different outlet pressure.

higher than that of the *homogeneous(c)* case (375 mA cm^{-2}), a 16.8% difference. For oxygen mass fraction at 0.025, the predicted current density for the *homogenous(c)* and the *non-homogeneous* case is 849 and 1040 mA cm^{-2}, respectively, or a 22.5% difference. The difference in current density is a result of differing oxygen diffusion rates due to the different GDL porosity used in the case.

4.2. Cross-channel flow due to pressure difference

Predicted polarization curves for different cathode outlet pressure ranging from 1 to 3 kPa are shown in Fig. 12 with intervals of 1 kPa. The outlet pressure of the anode channels is kept the same. The polarization curves show that cell performance increases with increasing of cathode outlet pressure difference, e.g. at 0.6 V the current density for $\Delta P_C = 1$, 2, and 3 kPa is 1084, 1114, and 1148 mA cm^{-2}, respectively. At higher load conditions, the current density increases slightly with increasing both cathode outlet pressure. The reason for is because of the convection induced by the pressure difference between two adjacent channels that introduces more reactant gas into the rib area. Fig. 13 shows the velocity vector on the X–Y plane and mass fraction of water vapor contour at $Z = 0.025$ m for the *non-homogeneous* cases with a pressure differential between two channels. Computational results of zone B of Fig. 4(b) are shown in this figure. Compared with the non-homogeneous case with no pressure difference (right-half portion in Fig. 8), the case with a $\Delta P_C = 2$ kPa clearly shows a gas flow through the rib area. This cross-channel flow helps to increase the reactant concentration underneath the rib area, hence an increase of limiting current.

Fig. 14 compares the prediction of current density distribution on the cathode catalyst layer for the non-homogeneous case without (Fig. 12a) and with (Fig. 12b) a pressure difference between channels. When there is no cross-channel flow, the current density distribution appears to be symmetrical with respect to the centerline of the cathode channel, cf. Fig. 14(a). The density current contours appear parabolic downstream in this case peaks at $X = 0.0165$ m and from that point on the current density decays towards the outlet, primarily due to depletion of oxygen downstream. When a convective cross-channel flow occurs due to pressure difference, the current density distribution on the high-pressure channel (right channel in Fig. 14(b) is shifted towards the rib/channel boundary. However, the current density contours in the left channel remain fairly symmetrical, showing only slight displacement to the left side. Notably, the current density peaks at similar axial location but the maximum value exceeds the baseline case, which has no pressure difference in the channels.

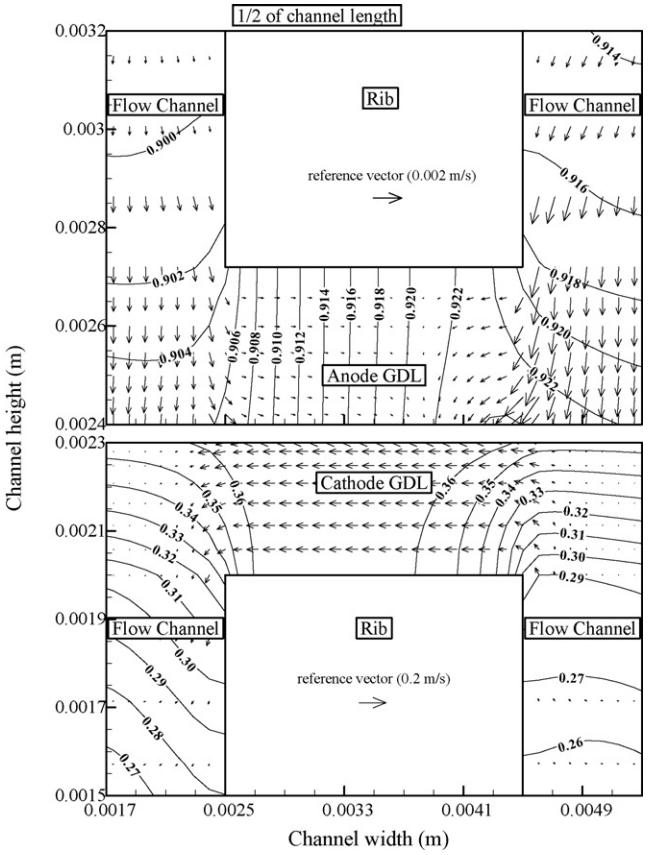

Fig. 13. Predicted velocity vector and mass fraction of water vapor ($Z = 0.025$ mm) in the non-homogenous case with $\Delta P_C = 2$ kPa.

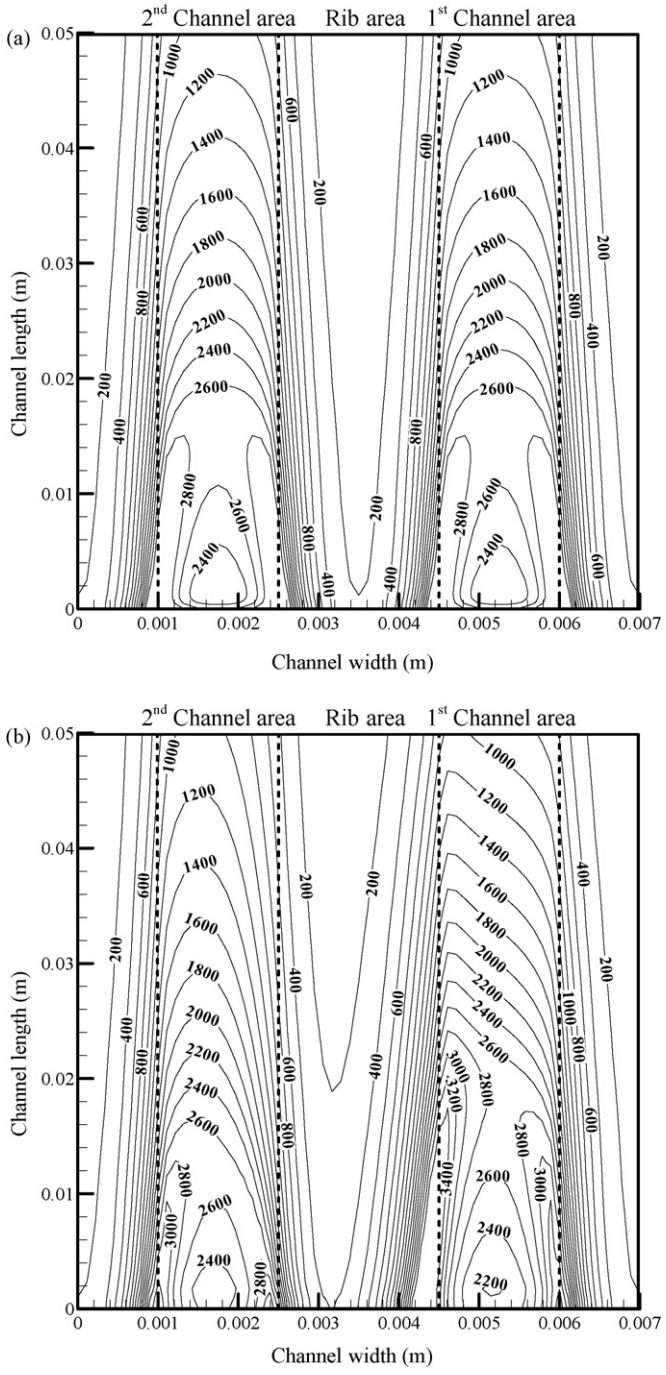

Fig. 14. Current density distribution at the cathode catalyst layer for two different non-homogeneous cases: (a) $\Delta P_C = 0$ kPa; (b) $\Delta P_C = 2$ kPa.

5. Conclusions

The present study reports on numerical investigations on the effect of compression force on the performance of PEM fuel cells. Experimental data of porosity and permeability for uncompressed and compressed GDL are used in the computation. The analysis focuses on the transport phenomenon of flow and reactant gases in GDL regions underneath the rib and the channel area. A 3D numerical model consisting of two parallel, straight channels along with an MEA and bipolar plates are constructed to study the problem. A series of numerical simulations are carried out to investigate the distribution of GDL properties on cell performance and to study the effects of cross-channel flow induced by a pressure gradient between the gas channels. The following conclusions were obtained:

(1) The polarization for the cases tested (*homogeneous(c)*, *homogeneous(u)*, and *non-homogeneous* cases) shows that cell performance for the configurations tested is controlled by the transport under the channel area. Therefore the limiting current density depends on the porosity assigned for this portion of the GDL. The predicted cell performance is *homogeneous(u)* > *non-homogeneous* > *homogeneous(c)*.
(2) In the *non-homogeneous* case, a highly non-uniform current density exists near the corner of the rib where hot spots may develop during operation. Therefore, careful and appropriate application of the compression force as well as rib/channel dimensions and geometry are required in order to avoid the formation of hot spots inside the MEA.
(3) When the pressure difference between two adjacent channels is high enough, a convective cross-channel flow occurs. A prediction of the effect of the cross-channel flow shows that the flow can bring more reactant gas into the rib region and improve the overall mass transport. This demonstrates the importance of accurate permeability values used in the numerical simulation for the rib (compressed) portion of the GDL.
(4) The cross-channel flow also affects the current density distribution. For the cases tested, it is found that the peak current density occurs in the high-pressure channel towards the rib/channel boundary near the channel with a low pressure.

Acknowledgment

The authors wish to thank Mr. Hong-Da Chang for the technical support of the SEM in Touch Micro-system Technology Inc.

References

[1] C.S. Kong, D.-Y. Kim, H.-K. Lee, Y.-G. Shul, T.-H. Lee, J. Power Sources 108 (2002) 185–191.
[2] X. Cheng, B. Yi, M. Han, J. Zhang, Y. Qiao, J. Yu, J. Power Sources 79 (1999) 75–81.
[3] L.R. Jordan, A.K. Shukla, T. Behrsing, N.R. Avery, B.C. Muddle, M. Forsyth, J. Appl. Electrochem. 30 (2000) 641–646.
[4] L.R. Jordan, A.K. Shukla, T. Behrsing, N.R. Avery, B.C. Muddle, M. Forsyth, J. Power Sources 86 (2000) 250–254.
[5] V.A. Paganin, E.A. Ticianelli, E.R. Gonzalez, J. Appl. Electrochem. 26 (1996) 297–304.
[6] H.-K. Lee, J.-H. Park, D.-Y. Kim, T.-H. Lee, J. Power Sources 131 (2004) 200–206.
[7] S. Escribano, J.-F. Blachot, J. Etheve, A. Morin, R. Mosdale, J. Power Sources 156 (2006) 8–13.
[8] V. Gurau, M.J. Bluemle, E.S. De Castro, Y.-M. Tsou, J.A. Mann Jr., T.A. Zawodzinski Jr., J. Power Sources 160 (2006) 1156–1162.
[9] V. Gurau, M.J. Bluemle, E.S. De Castro, Y.-M. Tsou, T.A. Zawodzinski Jr., J.A. Mann Jr., J. Power Sources 165 (2007) 793–802.
[10] C. Lim, C.Y. Wang, Electrochim. Acta 49 (2004) 4149–4156.
[11] W.-K. Lee, C.-H. Ho, J.W. Van Zee, M. Murthy, J. Power Sources 84 (1999) 45–51.
[12] J. Ge, A. Higier, H. Liu, J. Power Sources 159 (2006) 922–927.
[13] S. Litster, D. Sinton, N. Djilali, J. Power Sources 154 (2006) 95–105.
[14] K. Tuber, D. Pocza, C. Hebling, J. Power Sources 124 (2003) 403–414.
[15] U. Pasaogullari, C.Y. Wang, J. Electrochem. Soc. 151 (2004) A399–A406.
[16] U. Pasaogullari, P.P. Mukherjee, C.Y. Wang, K.S. Chen, J. Electrochem. Soc. 154 (2007) B823–B834.
[17] T.F. Fuller, J. Newman, J. Electrochem. Soc. 140 (1993) 1218–1225.
[18] P.C. Sui, N. Djilali, J. Power Sources 161 (2006) 294–300.
[19] W. Sun, B.A. Peppley, K. Karan, J. Power Sources 144 (2005) 42–53.
[20] L. Ma, D.B. Ingham, M. Pourkashanian, E. Carcadea, J. Fuel Cell Sci. Technol. 2 (2005) 246–257.
[21] V. Gurau, H. Liu, S. Kakac, AICHE J. 44 (1998) 2410–2422.
[22] J.S. Yi, T.V. Nguyen, J. Electrochem. Soc. 146 (1999) 38–45.
[23] W. He, J.S. Yi, T.V. Nguyen, AICHE J. 46 (2000) 2053–2064.
[24] S. Um, C.-Y. Wang, K.S. Chen, J. Electrochem. Soc. 147 (2000) 4485–4493.
[25] Z.H. Wang, C.Y. Wang, K.S. Chen, J. Power Sources 94 (2001) 40–50.
[26] L. You, H. Liu, Int. J. Heat Mass Transfer 45 (2002) 2277–2287.
[27] V. Gurau, F. Barbir, H. Liu, J. Electrochem. Soc. 147 (2000) 2468–2477.
[28] H.-S. Chu, C. Yeh, F. Chen, J. Power Sources 123 (2003) 1–9.

[29] R. Roshandel, B. Farhanieh, E. Saievar-Iranizad, Renew. Energy 30 (2005) 1557–1572.
[30] P. Zhou, C.W. Wu, G.J. Ma, J. Power Sources 163 (2007) 874–881.
[31] P. Zhou, C.W. Wu, J. Power Sources 170 (2007) 93–100.
[32] T. Hottinen, O. Himanen, Electrochem. Commun. 9 (2007) 1047–1052.
[33] I. Nitta, T. Hottinen, O. Himanen, M. Mikkola, J. Power Sources 171 (2007) 26–36.
[34] T. Hottinen, O. Himanen, S. Karvonen, I. Nitta, J. Power Sources 171 (2007) 113–121.
[35] H.-P. Chang, C.-L. Chou, Y.-S. Chen, T.-I. Hou, B.-J. Weng, Int. J. Hydrogen Energy 32 (2007) 316–322.
[36] A. Jena, K. Gupta, Int. Nonwovens J., Fall (2003) 45–53.
[37] A. Jena, K. Gupta, Fluid Part. Sep. J. 4 (2002) 227–241.
[38] S. Mazumder, J.V. Cole, J. Electrochem. Soc. 150 (2003) A1503–A1509.